High carbon steel/Inconel 718 bimetallic parts produced via Fused Filament Fabrication and Sintering

P. Ferro, A. Fabrizi, F. Bonollo, H.S.A. Elsayed, G. Savio
University of Padova, Italy
paolo.ferro@unipd.it, http://orcid.org/0000-0001-8008-1557
franco.bonollo@unipd.it, http://orcid.org/0000-0002-7196-2886
alberto.fabrizi@unipd.it, http://orcid.org/0000-0002-7568-5804
hamada.elsayed@unipd.it, http://orcid.org/0000-0002-9818-4498
gianpaolo.savio@unipd.it, http://orcid.org/0000-0001-5858-1483

F. Berto
University of Rome, Italy
filippo.berto@uniroma1.it, http://orcid.org/0000-0001-9676-9970

ABSTRACT. The possibility of producing high carbon steel/Inconel 718 bimetallic parts via Fused Filament Fabrication and Sintering is explored. Compatibility of the two alloys with particular attention to elements interdiffusion through the interface as well as the effect of the deposition strategy were analyzed. Microstructural features, relative density and parts shrinkage were investigated, as well. Although first-tentative process parameters values were not sufficient to reach an acceptable material densification, a good bonding between Inconel 718 and carbon steel was observed, suggesting the potential to obtain sound bimetallic parts with a great range of material properties. Due to a difference in densification kinetics, sintering temperature was revealed to be the most critical process parameter to optimize to minimize porosity.

KEYWORDS. Additive Manufacturing, Fused Filament Deposition, Bimetallic material, Inconel 718, High carbon steel, Microstructure, Interdiffusion, Defects.

INTRODUCTION

Metal Additive manufacting is attracting attention of industrial and academic world for its tremendous potential in producing very complex parts. Its working principle is based on overlapping CAD defined layers, one by one, until the 3D part is built. In more common AM processes addressed to metallic materials, each layer is made of

metallic powder that is consolidated by a laser or electron beam that scans the powder bed with different strategies [1]. The rapid solidification of the melted powder induces a very fine microstructure that in some cases allows to improve the mechanical properties of the additively manufactured component compared to those that are typical of subtractively manufactured ones [2]. Other advantages, among the others, are the topological optimization of load bearing components and the reduction of scraps. However, there are disadvantages, as well, such as solidification defects (say, porosity [3]), high surface roughness, distortion and residual stresses that can compromise the component performance and, even worst, its production [1]. In addition to powder bed fusion (PBF) additive manufacturing processes [4], there are different other alternative technologies belonging to the so called 'mainstream commercial metal AM technologies' that were developed. They are Directed Energy Deposition (DED) [5] and Binder Jetting (BJ) [6]. But, surprisingly, the list could go further with emerging new additive technologies such as Ultrasonic Additive Manufacturing (UAM) [7] and Metal Droplet Printing (MDP) [8]. In UAM the component is built up through the stacking and joining of solid metal strips by ultrasonic welding, while MDP is based on drop-on-demand ejection and liquid droplet deposition on a moving substrate. In all these techniques, the facility is highly expensive, the heating source has a low efficiency (above all dealing with laser, electron beam and friction) and the process time is not competitive with that of other subtractive technologies or casting processes. This is why one of the most important goals to reach in the field of AM technologies is to find out a strategy allowing significant reduction of process time and cost. In this scenario Fused Filament Fabrication and sintering (FFFS) could be a promising AM technique with the potential to reach the above-mentioned objectives [9]. A filament made of metallic powder embedded in a polymer (binder) is extruded to produce the 3D part, called 'green' part, by deposition as shown in Fig. 1.
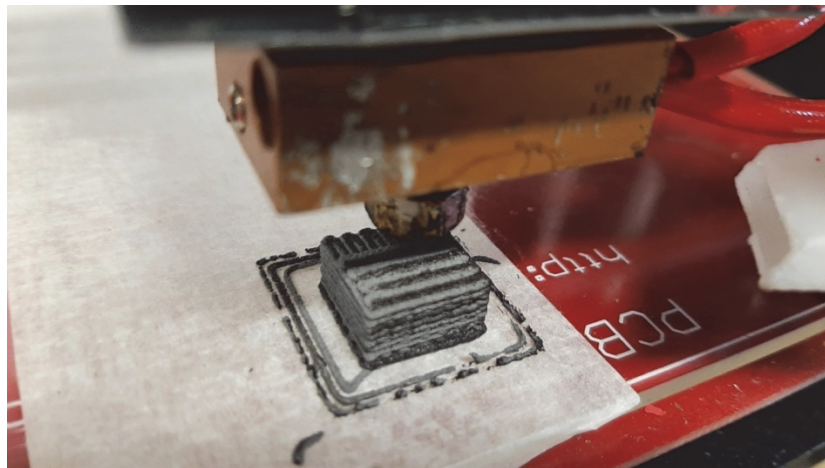

Figure 1: Green part production by Fused Filament Fabrication.

The green part undergoes then a chemical and/or thermal debinding which main goal is to eliminate the binder. This is a very critical step since a compromise is required between the amount of residual binder required to maintain the powder consolidation and the necessity to avoid alloy contamination. After debinding, the part is called 'brown' part. It finally undergoes a sintering heat treatment which temperature and holding time are alloy dependent [10]. It is worth mentioning that such AM technique is also called in literature Printing-Debinding-Sintering (PDS) [11], Fused Deposition Modeling and Sintering (FDMS) [12], Atomic Diffusion Additive Manufacturing (ADAM) [13] or Bound Metal Deposition (BMD) [14]. Due to the low filament extrusion energy during 3D printing and the possibility to carry out debinding and sintering on entire batches, FFFS shows great promise in the large-scale manufacturing of metal components at relatively higher fabrication rate and lower manufacturing cost [15].

Despite such advantages, the research aimed at improving the FFFS AM process is still at the early stage. Some pioneering works deal with the production of stainless steels or Nickel based alloys components via Fused Deposition Modeling and Sintering (FDMS). In a recent work, Liu et al. [12] investigated the possibility to produce AISI 316L Stainless Steel (SS) parts via FDMS. Brown Parts were first obtained through catalyst debinding at 120 °C for 8 h under nitrogen whose rate was 1 L/h and then by a heat treatment at 600 °C for 2 h to eliminate the residues inside the part. The sintering was carried out at 1360 °C for 2 h under the protection of argon. The porosity was found to be 7.77 % which is quite high for a metal part. Mechanical properties were in fact lower than those obtained with other manufacturing techniques so that authors concluded by claiming that FDMS is not suitable to fabricate structural parts but only functional products. Some year before,

Thomson et al. [15], using the same alloy (AISI 316L) to produce 3D printed parts via FFFS, reached better results in terms of porosity reduction. Thermal debindig was carried out for 90 min at 750 °C, temperature reached with a heating critical rate of 0.2 °C/min required to give time the polymer to escape and prevent defects formation. Sintering at 1360 °C for 2 h allowed to obtain densified parts with a porosity lower than 5%. However, FFFS was still recommended for fabrication of complex shaped metal parts for application with a focus on material functionality rather than structural components production. Better results, in terms of relative density, were obtained by Wang et al. [11] who studied the sintering mechanism that occurs during extrusion-based additive manufacturing of stainless steel (316L) via molecular dynamics simulation. The mechanism of Cr element aggregation at the grain boundaries was revealed by analysing the evolution of particle structure, diffusion activation energy, and interactions among solute elements during the heating process of Printing-Debinding-Sintering (PDS). Severe Cr aggregations at grain boundaries were reviled both numerically and by experiments. The extra energy released due to this aggregation phenomenon promoted a further coalescence of particles. A catalytic debinding was carried out using two temperature ramps that reached 433 °C and 573 °C, respectively. The cuboid samples subsequently underwent a pre-sintering heat treatment at 1010 °C and, finally, the sintering at 1327 °C. The relative density was 98.5%.

About nickel-based alloys, literature works focused above all on Inconel 718 (IN718). Thomson et al. [16] used an iterative process optimization to find the most suitable metal fused filament fabrication (MF³) process parameters to produce IN718 3D parts. They observed how the pick-up of impurities during debinding and sintering can result in the formation of carbides and oxides, often in form of prior particle boundaries (PPB) [17]. An acceptable concentration of grain boundary carbides can improve high-temperature strength. However, extensive amounts of high-temperature stable carbides can act as crack initiation sites, harming mechanical properties [18]. In the work of Thomson et al. [16], shaping was realized by combination of 3D fused filament printing and subsequent green body compression to eliminate minor printing defects. Removal of organic compounds was realized in a two-step debinding process, chemical and thermal (heating rate 1 °C/s between 170 °C and 550 °C). Finally, different sintering temperatures were tested, finding 1280 °C (holding time, 4h) the best one in term of material densification (>97%). Moreover, after a proper heat treatment, fabricated samples achieved mechanical properties similar to metal injection moulding (MIM) IN718 presented in literature.

Despite the numerous works about FFFS AM process, the use of such technique to produce bi-metallic materials was never explored in literature, to the best of the authors knowledge. As a matter of fact, there is the possibility to print the part by using two different filaments in co-extrusion or bi-extrusion regime, depending on whether each filament passes through the same nozzle (Cyclops hotend) or through a different nozzle (Chimera hotend).

The present work describes the first attempt to produce high carbon steel-IN718 bi-metallic parts via FFFS in co-extrusion regime with the aim to highlight unique phenomena occurring in bi-metallic material production, such as the alloy elements interdiffusion and drawbacks linked to different sintering rates. The choice of this couple of alloys derived above all from their similar sintering temperatures and the motivation to produce bimetallic parts with a unique combination of chemical, metallurgical and mechanical properties.

MATERIALS AND SAMPLES PRODUCTION

Cuboid specimens, size 10x10x10 mm³, were produced via co-extrusion of two filaments containing powder of Inconel 718 (IN718) and high carbon steel (HCS), respectively (Fig. 1). The nominal composition of the two alloys provided by the manufacturer, i.e. The Virtual Foundry is reported in Tab. 1.

IN718 filament, diameter 1.75 mm, contained nominally 87 wt% metal and had a density of 3.73 g/cm³; HCS filament had the same diameter and contained about 79.1% metal resulting in a density of 2.76 g/cm³. The polymer used in both filaments was polylactic acid (PLA).

Inconel 718 (nominal composition)				
Ni	Cr	Nb	Mo	Co
50-55	17-21	4.75-5.5	2.8-3.3	Max. 1.0
High carbon steel (measured with EDS)				
Fe	C	Si	Al	S & P
85.6	11.5	2.15	0.73	Bal.

Table 1: Chemical composition of the two alloys (wt%).

It is noted that the analysed HCS belongs to the family of hypereutectoid carbon steels.

The 3D printer used is a customized version of the Geetech Prusa i3 Pro B, with double extruder driven by two independent engines. It was equipped with a Rumba motherboard and an adapted Marlin firmware was compiled and installed. More details about the software can be found in the work by Sponchiado et al. [19].

'Co-extrusion' of the two different filaments means that both pass through the same nozzle (Cyclops hotend). In this condition the scanning strategy is directly linked to the resulted bi-material configuration (where 'configuration' means the geometrical disposition or layout of the two alloys inside the specimen). The co-extruded 'left-right' part is obtained by moving the nozzle with a horizontal path along the x-axis in the reference system schematized in Fig. 2a. The xy plane coincides with the 3D printer plate. The co-extruded 'top-bottom' cuboid is produced by shifting the nozzle along the y-axis with respect to the same reference system (Fig. 2b) and finally the 'crossed' co-extruded part is carried out by combining layer by layer the previous paths resulting in the configuration schematized in Fig. 2c.

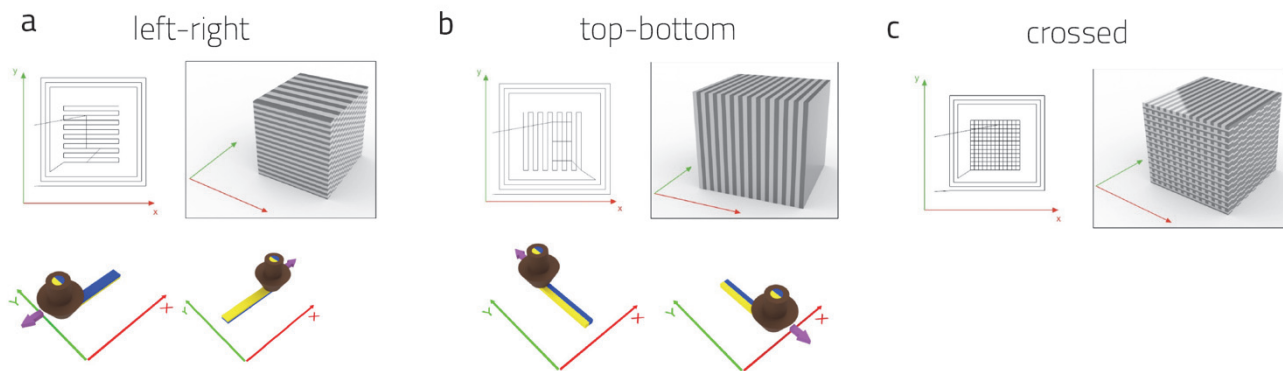Three samples for each scanning strategy were produced using the process parameters collected in Tab. 2.

Figure 2: Scanning strategies and derived configurations of co-extruded samples: (a) left-right, (b) top-bottom (c) crossed.

Layer height (mm)	Printing Speed (mm/s)	Nozzle Temperature (°C)	Bed Temperature (°C)	Extrusion width (mm)
0.4	15	210	50	0.8

Table 2: Used FFF process parameters.

After 3D printing, the green parts underwent to thermal debinding and sintering. Thermal debinding is a critical step since polymer must escape without compromising the structural integrity and geometry of the 3D printed part. For this reason, usually thermal debinding should involve two steps; the first (temperature one is design to eliminate the majority of polymer while avoiding the collapse of the part itself; the second one, at higher temperature, should allow the material densification to start while maintaining a certain degree of porosity to allow the residue of polymer to completely escape from the part. The melting and vaporization temperatures of PLA, 280 °C and 380 °C, respectively, were evaluated through differential scanning calorimetry (DSC) tests carried out with DSC 3+ Mettler Toledo. Therefore, the debinding temperature was chosen to be 450 °C (holding time, 2h) after a pre-heating at 200 °C for 2h and a heating rate of 1.5 °C/min. The temperature of pre-sintering (600 °C) was reached with the same heating rate and maintained for 2h. Finally, the sintering was carried out at 1280 °C, temperature that was reached with a heating rate of 5.5 °C/min and maintained for 4h. Slow cooling rates were used (1.9 °C/min up to 600 ° and 5 °C/min up to room temperature) to avert distortions or cracks. It is worth noting that Kloeden et al. [20] suggested, for IN718, sintering temperatures in the range between 1260 and 1290 allowing liquid phase sintering that promotes the highest material density. Moreover, since the filaments producer suggests 1300 °C as sintering temperature of HCS, it was decided, as fist tentative, to select as sintering temperature of the bimetal part, 1280 °C.

A vacuum cleaning followed by a flux of inert atmosphere, made of Ar (99.99%, 100 SCCM), was used to prevent oxidation inside the tubular sintering furnace (Zetasinter by Nanone) and allow the residues of polymer to escape. Moreover, no steel blend was used but the samples were simply placed on a refractory basal layer. Both filaments and samples were investigated by using electron scanning microscope (QUANTA FEG 250) equipped with Energy Dispersive Spectroscopy (EDS). Eventually, a chemical etching (Nital 3%) was used to reveal the microstructure. The mass of the samples before and after heat treatment was measured by weighing using a high precision electronic balance by ZEISS.

RESULTS AND DISCUSSION

Filaments analysis

Cuboid specimens, size 10x10x10 mm³, were produced via co-extrusion of two filaments containing powder of Inconel 718 (IN718) and high carbon steel (HCS), respectively (Fig. 1). The powder particles morphology and size are shown in Fig. 3.
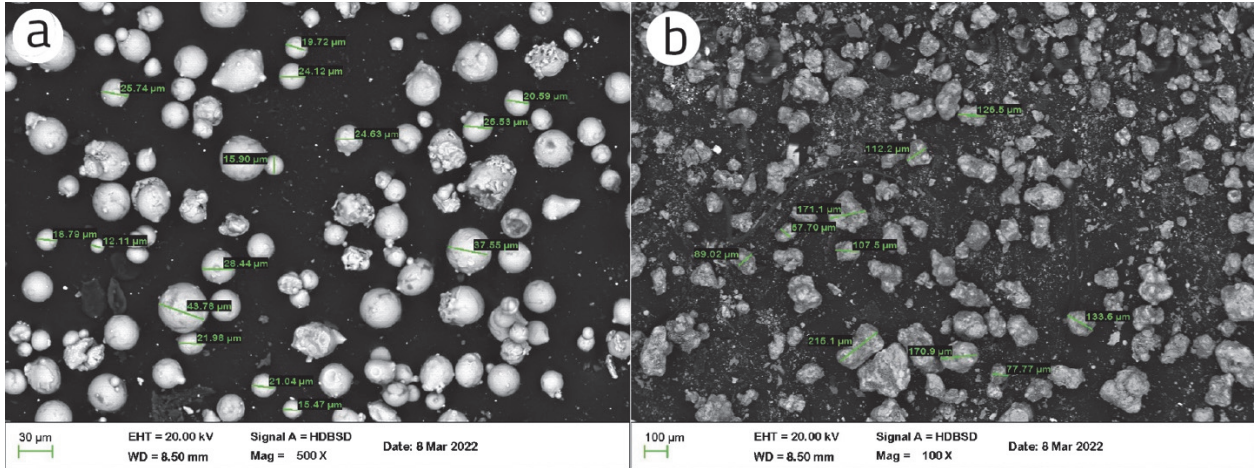

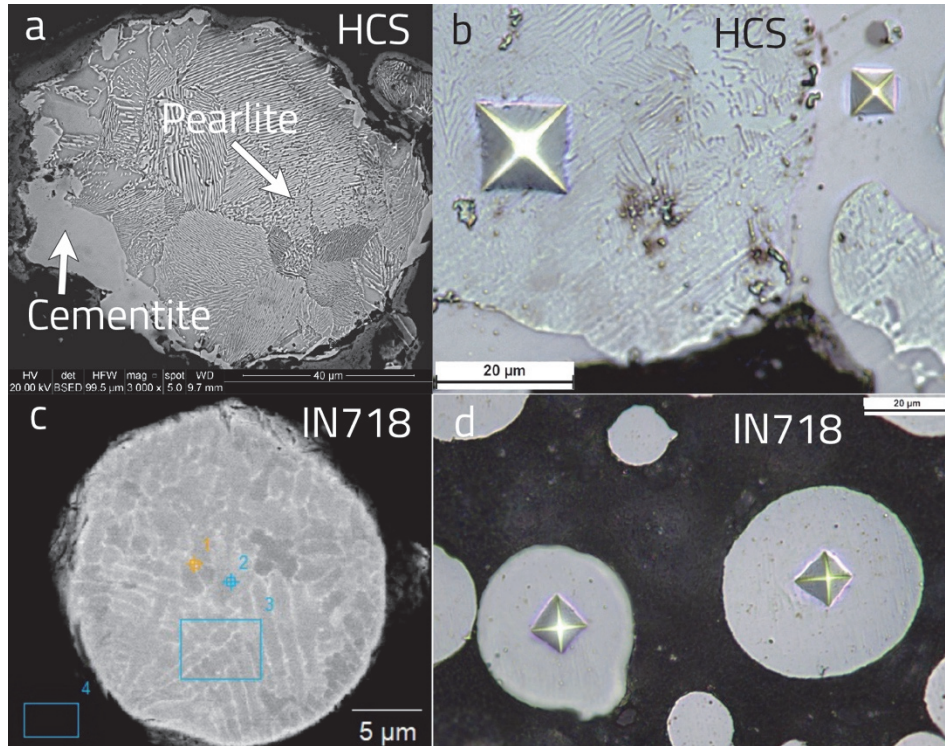Figure 3: Size and shape of powder particles: (a) IN718, (b) HCS.

Figure 4: Microstructure of powder particles: (a,b) HCS, (c,d) IN718.

It is observed a great difference in particles size and shape of the two alloys. While IN718 particles are spherical with size ranging from 15 to 40 µm (Fig. 3a), HCS particles are characterized by an irregular shape and size ranging from 80 to 200 µm. Despite the binder plays a principal role in the printing process so that the requirement on the morphology of the dispersed metal particles, including the sphericity, fluidity, and size distribution, is not as rigorous as that for selective laser melting (SLM) or other metal 3D printing methods, the evident difference in particle size between the two alloys could play a fundamental role in the subsequent heat treatment. A different sintering rate could characterize the two alloys not only because of their different chemical composition but also for their different shape and size. The higher the size the lower the driven force for densification given by the reduction of surface energy. Focusing on HCS particles microstructure, pearlite grains decorated by secondary cementite are observed (Fig. 4a). It was confirmed by Vickers microhardness measurements (Fig. 4b) which values resulted to be 320 ± 36 HV and 1318 ± 102 HV for pearlite and cementite, respectively. IN718 particles showed a dendritic structure with interdendritic segregations of heavy elements, such as Nb, as identified by EDS analysis of clear areas in Fig. 4c (Tab. 3). The Vickers microhardness (load 25 g) was 288 ± 17 HV.

	C	O	Al	Si	Ti	Cr	Fe	Ni	Nb	Mo
1	12.58	5.95	0.31	0.40	0.91	15.05	13.30	40.16	7.83	3.48
2	12.23	5.41	0.35	0.33	0.71	15.98	16.36	41.78	4.02	2.84
3	12.70	5.43	0.34	0.36	0.74	16.16	15.38	41.99	4.43	2.45
4	44.27	21.28	0.11	0.99	0.28	7.10	6.56	17.32	1.17	0.85

Table 3: EDS analysis of the IN718 particle shown in Fig. 4c.

Bimetal parts characterization
Fig. 5 shows some pictures at different magnifications of the green parts. Their initial volume and mass underwent a significant reduction after sintering as reported in Tab. 4. Moreover, they underwent a shape variation (Fig. 6) mainly due to the absence of steel blend during heat treatment that would have allowed a more uniform heating and cooling as well as a sort of structural support during debinding. A high grade of porosity was observed, as well, that revealed just a partial sintering of the parts (Fig. 6). This was attributed to a non-sufficiently high value of the sintering temperature and suggests that in bi-metal parts produced via FFFS, the more demanding material in terms of sintering temperature and holding time (say, HCS) dominates over the selection of process parameters.
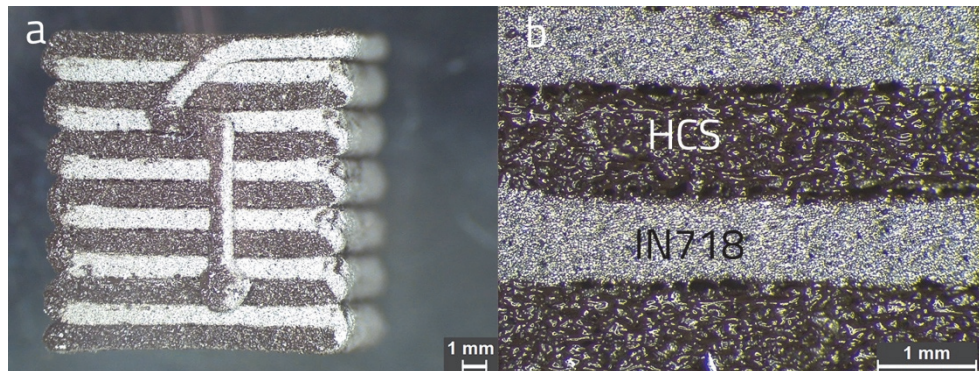

Figure 5: Green parts built with 'left-right' pattern.

Sample	Mass of green part [g]	Mass of sintered part [g]
'Left-right'	6.024	5.018
'Top-bottom'	5.589	4.644
Crossed	5.767	4.901

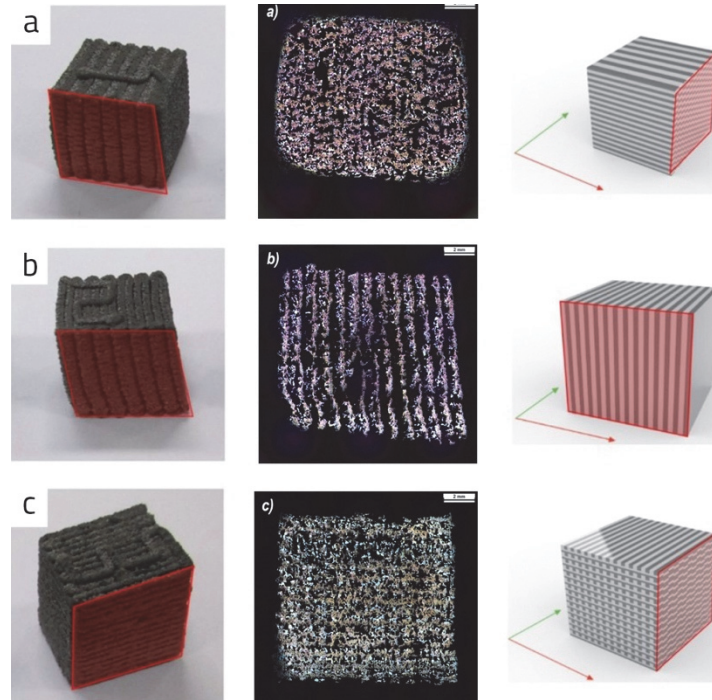Table 4: Mass before and after the heat treatment.

Figure 6: Macrographs of the FDMS part with red colored the surface observed: a) left-right, b) top-bottom, c) crossed.

IN718, that was the less demanding material in term of sintering temperature, showed a good grade of densification (Fig.7). However, each particle is decorated by a secondary phase rich in chromium and molybdenum, as proved by the EDS analysis reported in Tab. 5.
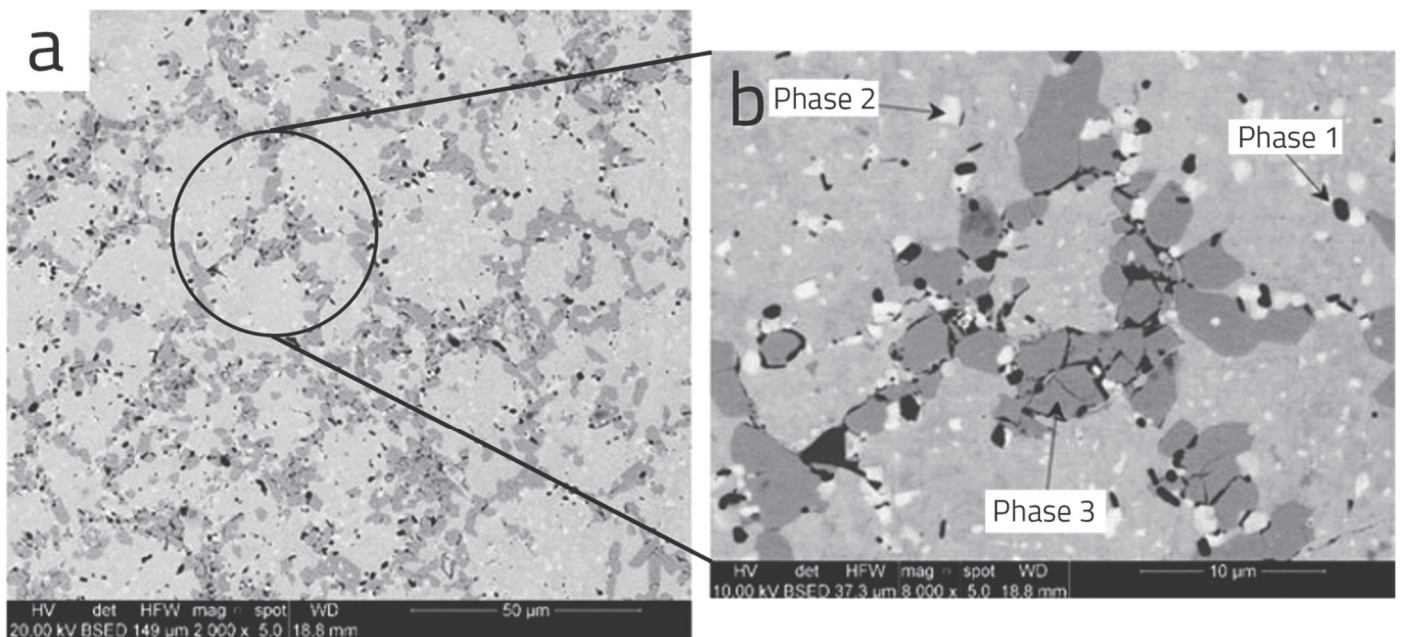

Figure 7: SEM micrographs of sintered IN718 powder at different magnifications

	C	O	Al	Si	Ti	Cr	Fe	Ni	Nb	Mo
Phase 1	3.02	**16.25***	**19.05***	0.77	0.74	8.18	24.60	22.49	3.32	1.57
Phase 2	4.52	6.06	0.24	0.73	**3.94***	8.09	18.77	16.46	**35.34***	**5.85***
Phase 3	4.14	3.35	0.27	0.71	0.51	**31.20***	30.41	23.21	2.30	**3.91***
Matrix	2.49	3.70	0.26	1.04	0.44	8.10	33.93	46.49	2.03	1.51

*Since EDS is a semi-quantitative analysis, numbers in bold simply highlight the differences against the matrix composition

Table 5: EDS analysis of IN718 sintered powder shown in Fig. 7b.

As observed by Wang et al. [11], Cr tends to segregate at the particle grain boundaries. They found that the cohesive interactions between Cr atoms were stronger than those of Fe and Ni elements during the final holding stage in their molecular dynamics (MD) simulation. The energy released by Cr aggregation further promoted the coalescence of particles and the stability of sintering body. Cr dot mapping showed a higher concentration of dotting points at the grain boundaries, and the point analysis also indicated an increase in the weight percentage of the Cr element at the grain boundaries. Therefore it supposed that carbon residue at the particle surface reacted with such Cr agglomerations producing Cr(Mo) carbides. Other secondary phases were identified by EDS analysis (Tab. 5) as oxide particles (black small particles in Fig. 7b) and Leaves phase (Ni,Cr,Fe)2(Nb,Mo,Ti) (white particles in Fig. 7b). In HCS zones, sintering didn't occur as clearly observed in Fig. 8. Such issue was mainly attributed to the sintering temperature that was found to be inadequate for the purpose. As a matter of fact, such parameter should be also calibrated according to the particles size that was significantly higher than that of IN718 particles. Moreover, it is worth noting that the observed high porosity grade can be also attributed to a non-homogeneous sintering kinetics. Due to the non-appropriate temperature and larger particles size of HCS, the sintering kinetics of HCS can be supposed slower than that of IN718, causing a sort of porosity induced by differential shrinkage.
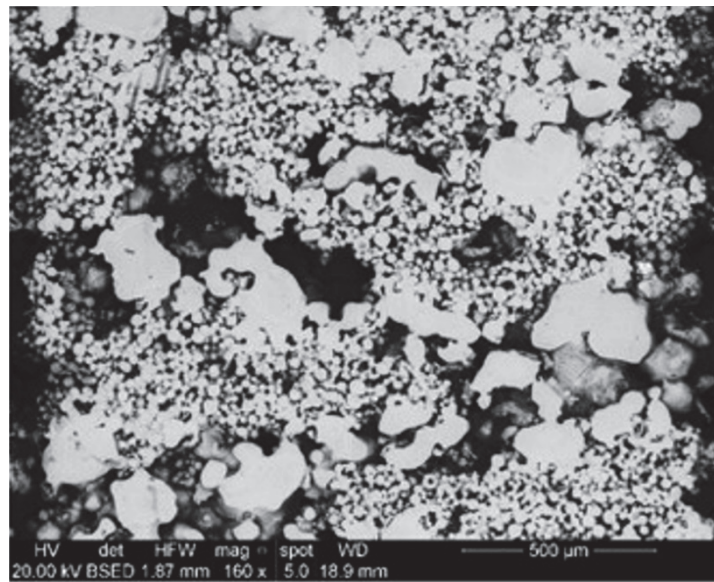

Figure 8: SEM micrograph of left-right FFF AM part.

Dealing with HCS particles, partially sintered with IN718, a very complex stratified microstructure was observed (Fig. 9) and attributed to an interdiffusion phenomenon at the interface between the two alloys. As Ni and Cr diffuse toward the HCS particles, which microstructure is fully austenitic at the sintering temperature, the steel becomes richer and richer of alloys elements modifying progressively the chemical composition and therefore the Continuous Cooling Transformation (CCT) curves position. It is well known that the higher the amount of alloys element the more the CCT curves moves toward right. Keeping this in mind and supposing the entire HCS particle undergoes the same cooling rate, where Ni and Cr were not able to reach the steel, the microstructure resulted to be made of equiaxed grains of pearlite. As the Ni and Cr content start to increase, austenite tends to transform into acicular phases (Fig. 9b). Where the Ni content results sufficiently high, the austenitic microstructure tends to stabilize similarly to austenitic stainless steels. A linescan across a HCS granule was performed to support this interpretation of the microstructure (Fig. 10).
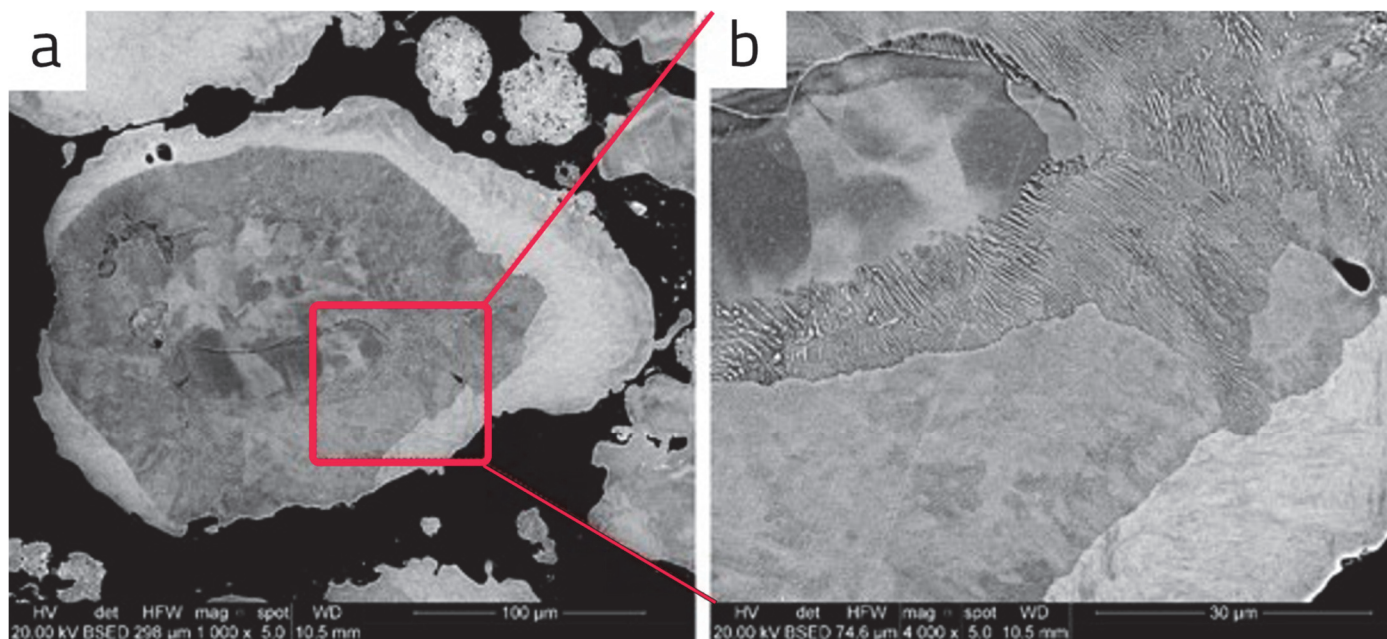
Figure 9: SEM micrographs of partially sintered HCS powder in touch with IN718 particles
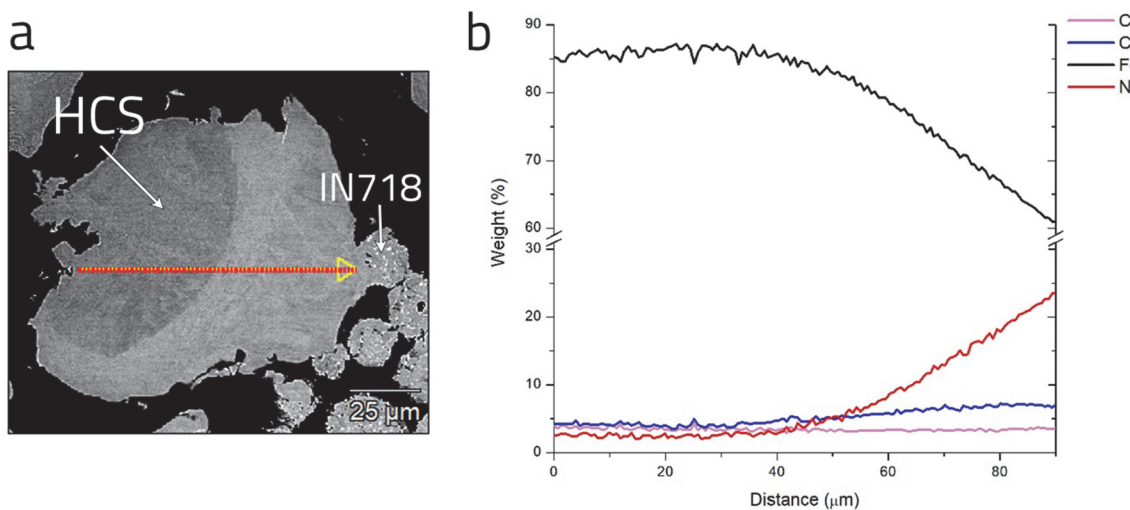

Figure 10: HCS particle in touch with IN718: a) SEM micrograph, B) EDS line scan across HCS.

As expected, it is shown a gradually increase of Ni and Cr moving from the HCS granule core toward the interface. Moreover, it is observed that the light gray phase in Fig. 10a starts to form as Ni begins to increase (Fig. 10b) and Fe to decrease.

CONCLUSIONS

Inconel 718/high carbon steel bimetallic samples were produced via fused filament fabrication and sintering. Despite in a first production tentative, a high porosity grade was observed, the obtained experimental results allow to highlight the main metallurgical phenomena involved in their production and that will be optimized in a future work. Sintering temperature (1280 °C) was revealed the most critical process parameter. It resulted sufficient for IN718 but inadequate for HCS, suggesting that such parameter should be selected by considering the more demanding material between the two alloys. In the present bi-metallic parts, the sintering temperature should exceed at least 1300 °C (HCS sintering temperature) despite the possible excessive liquid phase formation at grain boundary of IN718 and therefore the

risk of shape instability throughout the process. In this regard, the green parts should be completely dipped in steel blend during the heat treatment with the aim to contain the distortion of the parts during the debinding and sintering. Another important phenomenon to take into account is the *sintering kinetics mismatch* between the two alloys due to both single alloy chemical composition and particles size. The higher the particle size the longer the sintering time. This phenomenon causes a different alloy shrinkage and therefore could be a source of porosity at the interface between the two coupled alloys.

About alloys microstructure, different secondary phases (i.e.: Leaves phases) were detected in sintered IN718 powder, while, a stratified microstructure was observed in partially sintered HCS and IN718 particles due to Ni and Cr diffusion toward the steel granules.

Finally, this work establishes the bases for the combination of metals in FFFS and it is part of a wider research that aims at exploring the opportunity offered by multi-material additive manufacturing and its implications on design methods.

ACKNOWLEDGMENTS

REFERENCES

[1] Ferro, P., Berto, F. and Romanin, L. (2020). Understanding powder bed fusion additive manufacturing phenomena via numerical simulation, Frattura ed Integrità Strutturale, 14(53), pp. 252-284. DOI: 10.3221/IGF-ESIS.53.21.

[2] Razavi, S.M.J., Ferro, P., Berto, F., Torgersen, J. (2018). Fatigue strength of blunt V-notched specimens produced by selective laser melting of Ti-6Al-4V, Theoretical and Applied Fracture Mechanics, 97, pp. 376-384. DOI: 10.1016/j.tafmec.2017.06.021.

[3] Ferro, P., Savio, G., Meneghello, R., Berto, F. (2020). A modified volumetric energy density-based approach for porosity assessment in additive manufacturing process design. The International Journal of Advanced Manufacturing Technology, 110, pp. 1911–1921. DOI: 10.1007/s00170-020-05949-9.

[4] Bobbio, L.D., Qin, S.P., Dunbar, A., Michalerisc, P., Beesea, A.M. (2017). Characterization of the strength of support structures used in powder bed fusion additive manufacturing of Ti-6Al-4V, Addit. Manuf. 14, pp. 60–68. DOI: 10.1016/j.addma.2017.01.002.

[5] Tan, H., Fan, W., Qian, Y.H., Chen, Y.G., Liu, S.Q., Lin, X. (2020). Influence of inclined substrate on process characteristics of directed energy deposition, Opt. Laser Technol. 129, 106288. DOI: 10.1016/j.optlastec.2020.106288.

[6] Roberts, J.W., Sutcliffe, C.J., Green, P.L., Black, K. (2020). Modelling of metallic particle binders for increased part density in binder jet printed components, Addit. Manuf. 34, 101244. DOI: 10.1016/j.addma.2020.101244.

[7] Bourmias-Varotsis, A., Han, X.X., Harris, R.A., Engstrøm, D.S. (2019). Ultrasonic additive manufacturing using feedstock with build-in circuitry for 3D metal embedded electronics, Addit. Manuf. 29, 100799. DOI: 10.1016/j.addma.2019.100799.

[8] Liu, M.L., Yi, H., Cao, H.J., Huang, R.F., Jia, L. (2021). Heat accumulation effect in metal droplet-based 3D printing: evolution mechanism and elimination Strategy, Addit. Manuf. 48,102413. DOI: 10.1016/j.addma.2021.102413.

[9] Agarwala, M.K., Mukesh, K., van Weeren, R., Bandyopadhyay, A., Safari, A., Danforth, S.C., Priedeman, W.R., 1996. Filament feed materials for fused deposition processing of ceramics and metals. 7th Solid Freeform Fabrication Symposium, pp. 451–458.

[10] Gonzalez-Gutierrez, J., Cano, S., Schuschnigg, S., Kukla, C., Sapkota, J., Holzer, C. (2018). Additive manufacturing of metallic and ceramic components by the material extrusion of highly-filled polymers: a review and future perspectives, Mater. 11, pp. 840-876. DOI: 10.3390/ma11050840.

[11] Wang, F., You, S., Jiang, D., Ning, F., 2022. Study on sintering mechanism for extrusion-based additive manufacturing of stainless steel through molecular dynamics simulation. Additive Manufacturing 58, 102991. DOI: 10.1016/j.addma.2022.102991.

[12] Liu, B., Wang, Y., Lin, Z., Zhang, T., 2020. Creating metal parts by Fused Deposition Modeling and Sintering. Materials Letters 263, 127252. DOI: 10.1016/j.matlet.2019.127252.

[13] Galati, M., Minetola, P., 2019. Analysis of Density, Roughness, and Accuracy of the Atomic Diffusion Additive Manufacturing (ADAM) Process for Metal Parts. Materials 12, 4122. DOI: 10.3390/ma12244122.

[14] Watson, A., Belding, J., Ellis, B.D., 2020. Characterization of 17-4 PH Processed via Bound Metal Deposition (BMD). In: TMS 2020 149th Annual Meeting & Exhibition Supplemental Proceedings. The Minerals, Metals & Materials Series. Springer, Cham.

[15] Thompson, Y., Gonzales-Gutierrez, J., Kukla, C., Felfer, P., 2019. Fused filament fabrication, debinding and sintering as a low-cost additive manufacturing method of 316L stainless steel. Additive Manufacturing 30, 100861. DOI: 10.1016/j.addma.2019.100861.

[16] Thomson, Y., Zissel, K., Förner, A., Gonzales-Gutierrez, J., Kukla, C., Neumeier, S., Felfer, P. (2022). Metal fused filament fabrication of the nickel-base superalloy IN 718. J Mater Sci 57, pp. 9541–9555. DOI: 10.1007/s10853-022-06937-y.

[17] Horke, K., Meyer, A., Singer, R.F. (2019) Metal injection molding (MIM) of nickel-base superalloys. Handbook of Metal Injection Molding. Elsevier, pp. 575–608.

[18] Klöden, B., Jehring, U., Weißgärber, T. et al (2010) High temperature properties of MIM processed superalloys. Powder Inject Mould Int 4, pp. 63–67.

[19] Sponchiado, R.; Rosso, S.; Dal Fabbro, P.; Grigolato, L.; Elsayed, H.; Bernardo, E.; Maltauro, M.; Uccheddu, F.; Meneghello, R.; Concheri, G.; Savio, G., 2023. Modeling Materials Coextrusion in Polymers Additive Manufacturing. Materials 16, pp 820-844. DOI: 10.3390/ma16020820.

[20] Kloeden, B., Weissgaerber, T., Kieback, B., Langer, I. (2013). The processing and properties of metal injection moulded superalloys. Powder Inject Mould Int PIM, 7, pp. 53–66.